Biomedical Signal Processing and Control 112 (2026) 108555

Contents lists available at ScienceDirect

Biomedical Signal Processing and Control

journal homepage: www.elsevier.com/locate/bspc

Automatic identification of neurodegenerative diseases with 3D point cloud-based analysis using geometric deep learning in OCT retinal images

Lorena Álvarez-Rodríguez [a], Ana Pueyo [b,c], Joaquim de Moura [a,*], Iván García Prego [a], Elisa Vilades [b,c], Elena Garcia-Martin [b,c], Clara I. Sánchez [d,e], Jorge Novo [a], Marcos Ortega [a]

[a] VARPA Group, Biomedical Research Institute of A Coruña (INIBIC), University of A Coruña, A Coruña, Spain
[b] Department of Ophthalmology, Miguel Servet University Hospital, Zaragoza, Spain
[c] Aragon Institute for Health Research (IIS Aragon), Miguel Servet Ophthalmology Innovation and Research Group (GIMSO) University of Zaragoza, Zaragoza, Spain
[d] Quantitative Healthcare Analysis (qurAI) Group, Informatics Institute, Universiteit van Amsterdam, Amsterdam, The Netherlands
[e] Biomedical Engineering and Physics, Amsterdam UMC Locatie AMC Department of Biomedical Engineering and Physics, Amsterdam, The Netherlands

ARTICLE INFO

Keywords:
Geometric deep learning
Neurodegenerative diseases
Optical coherence tomography
Retinal imaging
3D point clouds

ABSTRACT

Neurodegenerative diseases (NDDs) such as Alzheimer's (AD), Multiple Sclerosis (MS), and Parkinson's (PD) are becoming increasingly prevalent, requiring reliable biomarkers for early detection and monitoring. Retinal layers, as captured by Optical Coherence Tomography (OCT), offer a promising avenue for automated analysis via deep learning methods. This study explores the use of Geometric Deep Learning (GDL) techniques, which redefine input data, for these prevalent and clinically significant diseases screening using point clouds extracted from Retinal Nerve Fibre Layer (RNFL) and Ganglion Cell Layer (GCL-BM) contours. Three representative GDL architectures were applied to three different analyses: (I) differentiating all NDDs from a control group, (II) separating each NDD from the control group, and (III) performing multi-class classification among the diseases. Optimal point cloud sizes were also investigated. Results showed that in analysis (I), the GDL strategy achieved a high F1-score of 0.92 using only 512 3D points. In analysis (II), with 1,024, 4,096, and 1,024 3D points, it achieved F1-scores of 0.93, 0.94, and 0.97 for AD, MS, and PD, respectively. In analysis (III), multi-class screening reached a F1-score of 0.87. These results demonstrate the effectiveness of using subsampled point clouds for differentiating NDDs and suggest that GDL methods can enhance the efficiency of retinal layer analysis, offering improvements over current state-of-the-art techniques. This highlights the potential of GDL in processing retinal data and advancing NDD detection and classification, with top-performing results obtained using only around 8% of the total 3D points from a sample.

1. Introduction

Neurodegenerative diseases (NDDs) are increasingly prevalent, yet they still lack reliable biomarkers for fast, early, and accurate diagnosis as well as progression monitoring. This often leads to misdiagnoses, as many NDDs present with overlapping symptoms [1], preventing patients from receiving timely and appropriate treatments, which in turn worsens their quality of life and that of their caregivers. Examples of such diseases include Alzheimer's Disease (AD), Multiple Sclerosis (MS), and Parkinson's Disease (PD). The age of MS onset is usually between 20 and 40 years of age, causing prolonged sick leave and even disability in people of working age, with the consequent impact on health and social spending in countries. AD and PD primarily affect the elderly, making them some of the most common pathologies within this age group. As the global population ages, the prevalence of these diseases is expected to rise significantly [2–4]. By 2050, an estimated 131 million people worldwide will be living with AD [5], while PD is growing at a faster rate than any other NDD [6]. Additionally, MS is the most common non-traumatic disabling condition in young adults [7]. Thus, advancing research in neurodegenerative diseases is not only crucial to improving the quality of life for affected individuals, but also for addressing the broader societal impact of these disorders.

Innovation in this domain arises from various fields, including advancements in medical imaging and the automation of analysis

* Corresponding author.
E-mail addresses: lorena.alvarezr@udc.es (L. Álvarez-Rodríguez), ana.pueyo@gmail.com (A. Pueyo), joaquim.demoura@udc.es (J. de Moura), ivan.garcia.prego@udc.es (I.G. Prego), elisavilades@hotmail.com (E. Vilades), egmvivax@unizar.es (E. Garcia-Martin), c.i.sanchezgutierrez@uva.nl (C.I. Sánchez), jnovo@udc.es (J. Novo), mortega@udc.es (M. Ortega).

https://doi.org/10.1016/j.bspc.2025.108555
Received 26 December 2024; Received in revised form 3 June 2025; Accepted 7 August 2025
Available online 19 August 2025

through deep learning, which significantly accelerates processes and aids specialists. Since the retinal layers exhibit morphological changes associated with neurodegenerative diseases [8–11], Optical Coherence Tomography (OCT) has emerged as a valuable technique in neuro-ophthalmology for identifying potential biomarkers [12–16]. This non-invasive, fast, and accessible imaging modality generates high-resolution cross-sectional and volumetric images of the retinal structure, providing a detailed view of tissue morphology, which makes it particularly well-suited for morphological studies. OCT is already an established tool in ophthalmology [17–19], and recent studies have demonstrated its potential in detecting early biomarkers for the neurodegenerative diseases targeted in this work, with applications in early diagnosis and disease progression monitoring. In particular, the literature focus on the macular thickness of the retinal layers as an indication of morphological changes in the retina derived from the presence of neurodegenerative diseases [20–23]. However, this approach often compresses complex 3D morphological information into a simplified scalar value which may fail to capture some subtle but clinically meaningful anatomical variations. A more comprehensive characterization of disease-related patterns would require computational methods capable of processing the full spatial context. Such methods are inherently more complex, as they must integrate and analyse high-dimensional retinal data while preserving the anatomical relationships within and across layers.

Regarding the type of methods used in this domain, the most commonly applied deep learning techniques in OCT analysis rely on methods such as convolutional neural networks (CNNs) [24,25] and transformers [26–28], which process OCT data as individual B-scans or 3D volumes, either in raw form or with segmentation masks of the retinal layers. However, these approaches often suffer from processing redundant information, leading to increased demands on computational resources and time. Geometric Deep Learning (GDL) offers an alternative strategy by optimizing the way data is handled, aiming to reduce computational complexity while maintaining or even improving classification accuracy [29]. Besides, it offers a new way of modelling 3D objects, like the retina which is typically studied as a 2D map or a single scalar value. GDL has already shown success in other medical imaging domains, such as aneurysm detection in Time-of-Flight Magnetic Resonance Angiographs (TOF-MRA) [30], brain state evaluation using functional Magnetic Resonance Imaging (fMRI) [31], and catheter segmentation and tip detection in cerebral angiography [32]. In the context of OCT, GDL has shown promising results in the diagnosis of glaucoma [33].

Despite significant advances in deep learning and OCT imaging for NDD detection, existing methods continue to face challenges in terms of computational efficiency, scalability, and generalizability across multiple diseases. Most approaches focus on individual pathologies or rely on traditional deep learning models, such as CNNs, which demand considerable computational resources and are prone to processing redundant information. A common limitation lies in their reliance on thickness-based features, which reduce the rich 3D retinal anatomy to scalar measurements and may overlook subtle yet clinically meaningful structural variations.Thus, the application of 3D point clouds and GDL in the context of OCT imaging remains underexplored, especially for comprehensive screenings involving multiple neurodegenerative diseases. Preliminary results of this strategy were presented in [34], demonstrating the feasibility of using GDL for MS screening in OCT images.

Given this important gap in the literature, in this work, we present a novel framework for the identification of NDDs using 3D point cloud-based analysis with GDL applied to retinal OCT images. The proposed methodology, illustrated in Fig. 1, involves extracting point clouds from OCT images, subsampling them, and applying advanced GDL architectures to classify neurodegenerative diseases across various classification scenarios. We used well-established GDL architectures to isolate and fairly evaluate the contribution of our novel point-based retinal representation. Our method aims to automatically identify three of the most prevalent and clinically significant pathologies in this domain: AD, MS, and PD. To capture the most informative features, our framework leverages subsampled 3D point clouds of the superior and inferior contours of the Retinal Nerve Fibre Layer (RNFL) and the Ganglion Cell Layer together with Bruch's Membrane (GCL-BM), which have been shown to be relevant retinal layers for the analysis of these neurodegenerative diseases [25]. Rather than relying on scalar thickness descriptors, our approach captures the complete 3D spatial topology of these retinal surfaces, enabling the detection of nuanced morphological patterns and subtle structural deformations that may go unnoticed in traditional analyses. Moreover, the concept of thickness remains inherently integrated in our point cloud representation, as the distances between segmented surfaces naturally encode this information within a richer anatomical context. This strategy allows us to capture critical disease-related changes while minimizing redundancy, optimizing both accuracy and computational efficiency, which are key aspects for clinical translation.

Our contributions include:

- A novel fully automatic framework for the identification of three neurodegenerative diseases (AD, MS, PD) using OCT retinal images.
- The application and evaluation of three state-of-the-art 3D point cloud-based architectures for the analysis of retinal layers.
- The analysis of three different classification scenarios to evaluate disease separability: (a) classifying all NDDs as a single class versus a control group (b) assessing the separability of each NDD from the control group, and (c) performing multiclass classification for individual disease differentiation.
- A comprehensive analysis of classification performance across various point cloud sizes, demonstrating superior results compared to the traditional 3D CNN approaches.

This manuscript is organized as follows: Section 2 delineates the data and architectures utilized in this study, along with a detailed explanation of the experimental methodology. Section 3 presents the results, which are then commented on Section 4. Finally, Section 5 summarizes the key findings and conclusions of this research.

2. Materials and methods

2.1. Dataset

2.1.1. OCT dataset

Our source OCT dataset contains 1 555 raw OCT cubes from 4 different patient cohorts: 315 Healthy Controls (HC), 59 AD, 881 MS, and 300 PD samples. These samples belonged to 366 unique patients, distributed as follows: 87 HC, 29 AD, 167 MS, and 83 PD. Each volume was formed typically by 25 equally spaced 496×512 B-scans, having a total amount of 6,348,800 pixels to be analysed. Participants were prospectively recruited by three specialized clinicians: a neuro-ophthalmologist, a neurologist specializing in demyelinating diseases, and a neurologist specializing in movement disorders and dementia. Exclusion criteria for all participants included best-corrected visual acuity less than 0.5 (Snellen chart), refractive errors greater than 5 diopters of spherical equivalent or 3 diopters of astigmatism, intraocular pressure greater than 20 mmHg, and media opacities (nuclear colour/opalescence, cortical or posterior subcapsular lens opacity ≥ 2, according to the Lens Opacity Classification System III). In addition, patients with glaucoma, retinal diseases or systemic conditions affecting vision were excluded. All procedures followed the Declaration of Helsinki, and written informed consent was obtained from all participants. The study was approved by the Ethics Committee of Hospital Miguel Servet (CEICA: Comité Ético de Investigaciones Científicas de Aragón) with registration number C.I. PI21/113.

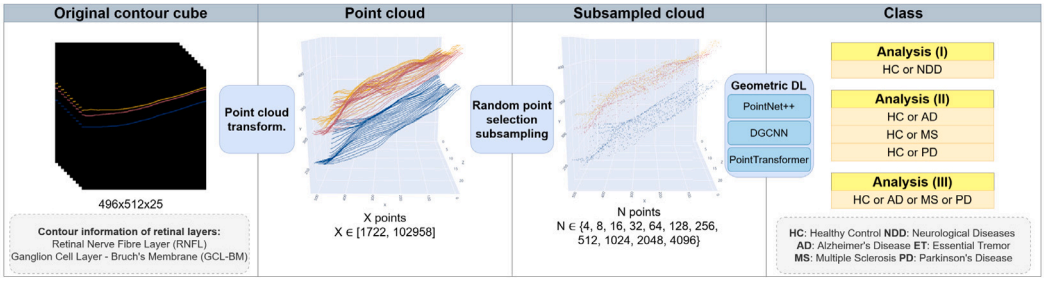

Fig. 1. Overview of the proposed methodology for the automatic identification of NDD using 3D point cloud-based analysis and GDL. The pipeline starts with the original OCT contour cube (496 × 512 × 25), from which point clouds are extracted. These clouds, with varying numbers of points (ranging from 1722 to 102,958), are then subsampled using random selection into point clouds of size N, where N takes values between 4 and 4096 points. The final step involves training the GDL architectures (PointNet++, DGCNN, and PointTransformer) on three different classification analyses: (I) NDDs vs. Healthy Controls (HC), (II) each individual NDD vs. HC, and (III) multi-class classification to separate the three NDDs from each other and from HC.

2.1.2. 3D point cloud dataset

The previous dataset had Retinal Nerve Fibre Layer (RNFL) and the Ganglion Cell Layer joint with Bruch's Membrane (GCL-BM) automatically segmented as in [35] using the framework nnUNet [36], which required anatomical consistency across subjects. As a result, all samples were already spatially aligned, requiring no further normalization or registration procedures. These areas of the retina show signs of affectation in the aforementioned diseases [37–42], and are therefore a convenient target in the search for computational biomarkers. Although these morphological alterations are often subtle and not easily discernible through direct visual inspection of raw OCT images, computational analysis can effectively capture nuanced yet clinically relevant patterns. To illustrate this, Fig. 2 presents representative examples of the dataset. Each volume was processed to extract only the limits of each layer from the complete cube, where limiting surfaces were formed by 2 pixels at most. Each contour pixel was converted into a 3D point, so the dataset comprises from 1722 to 102,958 points per case, being most commonly formed by 50,000 data points. The extreme values of the point clouds size occur due to the different amount of B-slices a cube can have, as well as the inclination of the layers which affect the amount of pixels belonging to the surface. In any case, this offers a rich foundation for exploring the pathological patterns manifested in the morphological changes of the layers targeted. Following extraction, a random subsampling step was applied uniformly and without replacement to reduce the point cloud size according to the experimental configuration. This process preserved the structural integrity and spatial distribution of the original data. In our methodology, each point cloud was reduced to multiple predefined sizes to support the efficiency study. Importantly, no additional preprocessing such as normalization or spatial realignment was required, as the standardized acquisition protocol and segmentation pipeline already ensured consistent anatomical orientation, scale, and alignment across all samples.

2.2. 3D GDL classification backbones

In this work, we opted for well-established GDL architectures as a foundation to assess the effectiveness of our proposed point cloud configurations and retinal layer representations. This choice prioritizes reproducibility and interpretability, enabling a clearer analysis of the methodological contributions without introducing potential variability from more recent, less validated models. By focusing on known baselines and combining them with novel point selection strategies tailored to retinal OCT, we isolate the added value of our geometric approach while laying the groundwork for future integration of newer architectures. Three point-cloud processing architectures were chosen in this work to be applied in the screening task: PointNet++ [43], Dynamic Graph CNN (DGCNN) [44], and PointTransformer [45]. PointNet++ is a hierarchical neural network that applies deep learning on point set recursively on a nested partitioning of the input point set that is able to learn local features with increasing contextual scales. It has been previously used for tasks such as medical feature points extraction for surgical procedures [46], femur parameter measurement [47], sleep pose classification [48], human identification based on tooth [49] or registration for middle ear diagnostics with endoscopic OCT [50]. DGCNN is based on the module EdgeConv, which incorporates local neighbourhood information; can be stacked or recurrently applied to learn global shape properties; and in multi-layer systems affinity in feature space captures semantic characteristics over potentially long distances in the original embedding. It has provided adequate results on tasks like lung fissures segmentation [51], brain network classification for depressive disorder [52], schizophrenia detection in fMRI [53] or epilepsy detection [54]. PointTransformer is transformer-based graph learning architecture known by its proven effectiveness in capturing both local geometric details and broader contextual information. It was used for MS screening [34], and its use would be further studied in our work as it is applied to different analysis and more NDD.

2.3. 3D CNN baseline architectures

Additionally, 3D classification CNNs are used to establish a baseline. Specifically, the 3D variants of EfficientNet [55], Squeeze-and-Excitation Network (SENet) [56] and DenseNet [57]. DenseNet has been applied in previous studies focused on HPV characterization in carcinoma CT images [58] and ovarian cancer monitoring based on PET/CT scans [59]. EfficientNet was used for COVID detection in X-ray [60], AD diagnosis in MRI [61] and lung cancer prediction [62]. SENet was applied to insect identification [63], superpixel segmentation [64] and histopathological image classification [65].

In our work, the 3D DenseNet-121, EfficientNet-B0 and SEResNet152 are trained under the same conditions as the GDL architectures for each analysis, ensuring a fair comparison between the approaches. These traditional methods process the whole OCT cube containing the complete contour segmentation masks for each B-scan, i.e. 6,348,800 pixels.

2.4. Training details

Regarding the training details of the models, training and test sets were split following a 90%–10% proportion. This initial training set was then randomly subdivided into training and validation set in a 80%–20% split. Each of these divisions was repeated 5 times to ensure the robustness of the experiment. Adam optimizer was used following a 1e−4 learning rate and Cross Entropy as loss function. Given the class imbalance, each was given a weight depending on its presence in the training set as given by $W(c) = \frac{N}{C*n_c}$, where N is the total amount of samples, C is the number of classes and n_c is the number of samples for a class c. GDL models were trained for 400 epochs and baseline models for 100 and 150 epochs for binary and multiclass approaches, respectively. We took the weights at the best epoch in terms of validation metric.

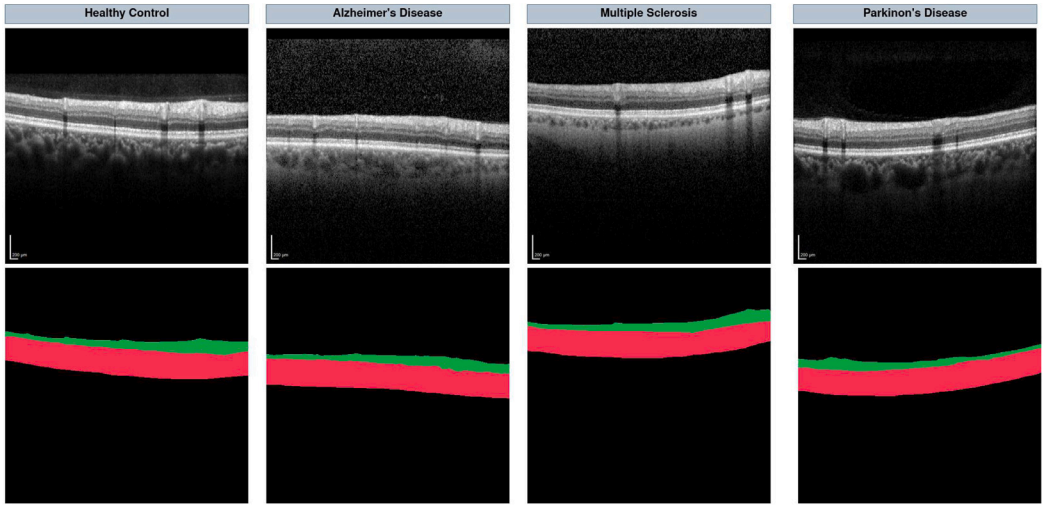

Fig. 2. B-scan examples with their corresponding annotations for each cohort in the dataset.

2.5. Hardware and software resources

Our implementation was based on Python 3.6.6 and PyTorch 1.10.2. Point cloud data was managed with PyTorch Geometric 2.0.3, and neuroimaging data with NiBabel 3.2.2. The hardware used was a machine powered by an Intel Xeon E5-2650 v4 CPU at 2.20 GHz, complemented with 505 GB of RAM for processing efficiency, with Debian GNU/Linux 10 as operating system. Graphics computations used a Tesla P100-PCIE 16 GB GPU. MONAI 1.3.0 was used for additional deep learning classification backbones.

3. Results

We conducted three experimental configurations to evaluate the separability of the pathologies at different levels: (I) all neurodegenerative diseases (NDDs) combined versus the healthy control group (HC), (II) each disease individually compared to the HC group, and (III) a multi-class classification where all disease cohorts were compared against each other. For each configuration, point clouds were randomly subsampled into 11 sizes, defined by 2^n, where $n \in [2, 12]$. Although the original point cloud sizes were much larger than the largest subsampling size, our experiments showed that increasing the number of points beyond $n = 12$ did not lead to any significant improvement in performance. Therefore, the maximum point cloud size was limited to $n = 12$. The following subsections provide detailed results for each experimental configuration. This experimental setup was intentionally designed to assess two core aspects of the proposed method: the influence of different GDL architectures and the effect of point cloud size on classification performance. By keeping other factors constant and avoiding extensive preprocessing or augmentation, we aimed to isolate the contribution of our point-based layer encoding strategy and preserve the clinical realism of the pipeline.

3.1. Analysis I: Neurodegenerative diseases cohort separability

This first analysis aims to determine whether a neuropathological cohort of patients can be accurately recognized by the selected backbones using different 3D point cloud sizes. The test results are presented in Table 1, where PointNet++ with 4096 points demonstrated the best performance in terms of classification metrics. Fig. 3 provides a clearer visualization of the F1-score, showing that while the optimal performance is achieved with 4096 points, comparable results can also be obtained with smaller configurations, such as 512, 1024, and 2048 points. Additionally, when smaller point cloud sizes are used, DGCNN outperforms the other architectures, whereas for larger configurations, PointNet++ is the superior model. PointTransformer consistently performs the worst across all settings. Finally, while the 3D CNN best baseline (DenseNet) outperforms most configurations, PointNet++ with 4096 points surpasses it in terms of classification metrics. In terms of time taken, it increases as more points are considered, specially for DGCNN.

3.2. Analysis II: Individual disease separability

In this analysis, each pathology is individually screened against the control group. Table 2 shows the test results for AD, where the top performing setting was PointNet++ with 1024 points, closely followed by the same architecture with 2048 points. By analysing with F1-score only as depicted in Fig. 4, slight stabilization in the metrics appear from 512 to 4096 points, which might indicate the introduction of redundant data. In this case, most of the GDL configurations outperform the best CNN baseline (DenseNet), particularly those above 16 points. Time taken for computation increases faster for DGCNN from 2048 points on.

Regarding MS, Table 3 depicts the test results obtained, where PointNet++ with the maximum size considered was the best performing setting. Slightly under are the 2048 and 1024 configurations, showing again the stabilization trend at 512 points, which is represented in Fig. 5, too. These bigger configurations are also slightly better than the best CNN baseline (DenseNet). In terms of time, it spikes at 4096 points for DGCNN, in a more marked way than in previous approaches probably due to the bigger size of the MS cohort.

As for PD, in Table 4 PointNet++ showed the best results with 4096 and 1024 points, being also similar to metrics with 2048 and 512 sizes. In Fig. 6 the same behaviour is observed in terms only of F1-score. These bigger settings, above 256 points, are also better than the best CNN baseline (DenseNet) for most classification metrics. Time evolves as in previous analysis.

3.3. Analysis III: All classes separability

For the third analysis, each class was considered individually at the same time in all versus all approach. The results are depicted in Table 5. The best results were achieved with PointNet++ and 4096 points, and these values are more similar to those seen before. Again, in terms of F1-score values shown in Fig. 7, similar top performing values are obtained once reached the 512 points minimum. With this variant the best CNN (DenseNet) results also improve, but from 128 points on the GDL approaches outperform this baseline, too. DGCNN is the architecture that spikes in terms of time in a more pronounced way, again due to the bigger size of the cohorts considered in this approach.

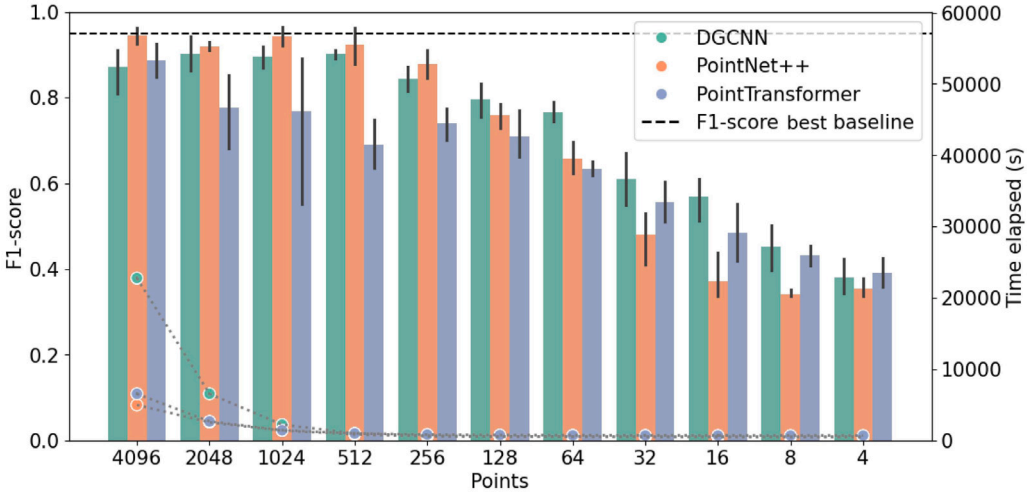

Fig. 3. F1-score mean and standard deviation (bars and vertical line) and time in seconds (points) for Analysis I: neurodegenerative diseases cohort separability. F1-score for the best configuration 0.95 ± 0.02, and for the best CNN baseline 0.95 ± 0.03.

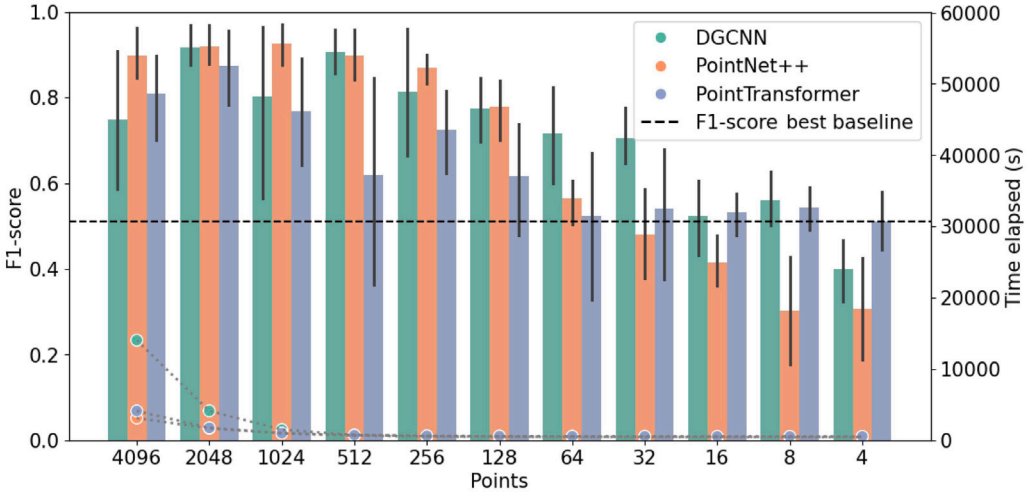

Fig. 4. F1-score mean and standard deviation (bars and vertical line) and time in seconds (points) for Analysis II: Individual disease separability, focused on AD. F1-score for the best configuration 0.93 ± 0.06, and for the best CNN baseline 0.51 ± 0.21.

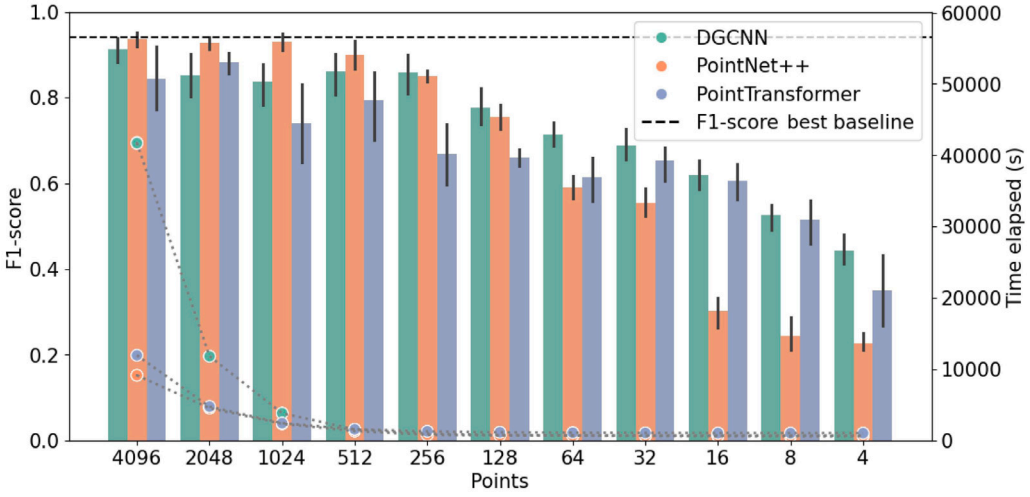

Fig. 5. F1-score mean and standard deviation (bars and vertical line) and time in seconds (points) for Analysis II: Individual disease separability, focused on MS. F1-score for the best configuration 0.94 ± 0.02, and for the best CNN baseline 0.94 ± 0.02.

Table 1
Test results for Analysis I: neurodegenerative diseases cohort separability.

Input size	Architecture	Accuracy	Precision	Recall	F1-score	AUROC
3*6,348,800 pixels	SEResNet152	0.79 ± 0.04	0.82 ± 0.01	0.94 ± 0.06	0.88 ± 0.03	0.73 ± 0.03
	EfficientNet	0.79 ± 0.01	0.80 ± 0.01	0.99 ± 0.01	0.88 ± 0.01	0.71 ± 0.02
	3D DenseNet161	0.92 ± 0.05	0.95 ± 0.06	0.97 ± 0.04	0.95 ± 0.03	0.97 ± 0.02
3*4,096 3D points	DGCNN	0.88 ± 0.06	0.90 ± 0.03	0.88 ± 0.06	0.87 ± 0.06	0.98 ± 0.01
	PointNet++	0.95 ± 0.02	0.95 ± 0.02	0.95 ± 0.02	0.95 ± 0.02	0.98 ± 0.01
	PointTransformer	0.89 ± 0.05	0.90 ± 0.04	0.89 ± 0.05	0.89 ± 0.05	0.97 ± 0.03
3*2,048 3D points	DGCNN	0.90 ± 0.05	0.91 ± 0.04	0.90 ± 0.05	0.90 ± 0.05	0.96 ± 0.02
	PointNet++	0.92 ± 0.01	0.92 ± 0.01	0.92 ± 0.01	0.92 ± 0.01	0.98 ± 0.02
	PointTransformer	0.79 ± 0.08	0.83 ± 0.04	0.79 ± 0.08	0.78 ± 0.09	0.93 ± 0.03
3*1,024 3D points	DGCNN	0.90 ± 0.03	0.90 ± 0.03	0.90 ± 0.03	0.89 ± 0.03	0.98 ± 0.01
	PointNet++	0.94 ± 0.03	0.94 ± 0.03	0.94 ± 0.03	0.94 ± 0.03	0.99 ± 0.01
	PointTransformer	0.80 ± 0.15	0.76 ± 0.25	0.80 ± 0.15	0.77 ± 0.22	0.95 ± 0.01
3*512 3D points	DGCNN	0.90 ± 0.01	0.91 ± 0.01	0.90 ± 0.01	0.90 ± 0.01	0.97 ± 0.02
	PointNet++	0.92 ± 0.05	0.93 ± 0.04	0.92 ± 0.05	0.92 ± 0.05	0.97 ± 0.02
	PointTransformer	0.71 ± 0.06	0.76 ± 0.06	0.71 ± 0.06	0.69 ± 0.06	0.86 ± 0.02
3*256 3D points	DGCNN	0.84 ± 0.03	0.85 ± 0.03	0.84 ± 0.03	0.84 ± 0.03	0.94 ± 0.01
	PointNet++	0.88 ± 0.04	0.89 ± 0.03	0.88 ± 0.04	0.88 ± 0.04	0.96 ± 0.02
	PointTransformer	0.75 ± 0.04	0.78 ± 0.03	0.75 ± 0.04	0.74 ± 0.04	0.84 ± 0.01
3*128 3D points	DGCNN	0.80 ± 0.04	0.82 ± 0.03	0.80 ± 0.04	0.80 ± 0.05	0.92 ± 0.03
	PointNet++	0.76 ± 0.04	0.78 ± 0.05	0.76 ± 0.04	0.76 ± 0.03	0.86 ± 0.04
	PointTransformer	0.72 ± 0.05	0.78 ± 0.03	0.72 ± 0.05	0.71 ± 0.06	0.82 ± 0.04
3*64 3D points	DGCNN	0.77 ± 0.03	0.78 ± 0.04	0.77 ± 0.03	0.77 ± 0.03	0.84 ± 0.04
	PointNet++	0.66 ± 0.04	0.68 ± 0.06	0.66 ± 0.04	0.66 ± 0.04	0.74 ± 0.04
	PointTransformer	0.65 ± 0.01	0.71 ± 0.05	0.65 ± 0.01	0.63 ± 0.02	0.76 ± 0.04
3*32 3D points	DGCNN	0.64 ± 0.05	0.72 ± 0.06	0.64 ± 0.05	0.61 ± 0.07	0.77 ± 0.04
	PointNet++	0.56 ± 0.03	0.57 ± 0.16	0.56 ± 0.03	0.48 ± 0.07	0.58 ± 0.05
	PointTransformer	0.60 ± 0.04	0.66 ± 0.05	0.60 ± 0.04	0.56 ± 0.06	0.69 ± 0.01
3*16 3D points	DGCNN	0.60 ± 0.04	0.64 ± 0.04	0.60 ± 0.04	0.57 ± 0.06	0.68 ± 0.04
	PointNet++	0.51 ± 0.01	0.31 ± 0.12	0.51 ± 0.01	0.37 ± 0.07	0.53 ± 0.05
	PointTransformer	0.56 ± 0.04	0.66 ± 0.10	0.56 ± 0.04	0.48 ± 0.08	0.60 ± 0.09
3*8 3D points	DGCNN	0.54 ± 0.04	0.58 ± 0.13	0.54 ± 0.04	0.45 ± 0.06	0.66 ± 0.04
	PointNet++	0.50 ± 0.00	0.30 ± 0.10	0.50 ± 0.00	0.34 ± 0.01	0.48 ± 0.10
	PointTransformer	0.53 ± 0.01	0.62 ± 0.04	0.53 ± 0.01	0.43 ± 0.03	0.54 ± 0.06
3*4 3D points	DGCNN	0.51 ± 0.01	0.49 ± 0.20	0.51 ± 0.01	0.38 ± 0.05	0.54 ± 0.06
	PointNet++	0.50 ± 0.01	0.37 ± 0.15	0.50 ± 0.01	0.35 ± 0.02	0.54 ± 0.08
	PointTransformer	0.49 ± 0.01	0.43 ± 0.09	0.49 ± 0.01	0.39 ± 0.04	0.52 ± 0.06

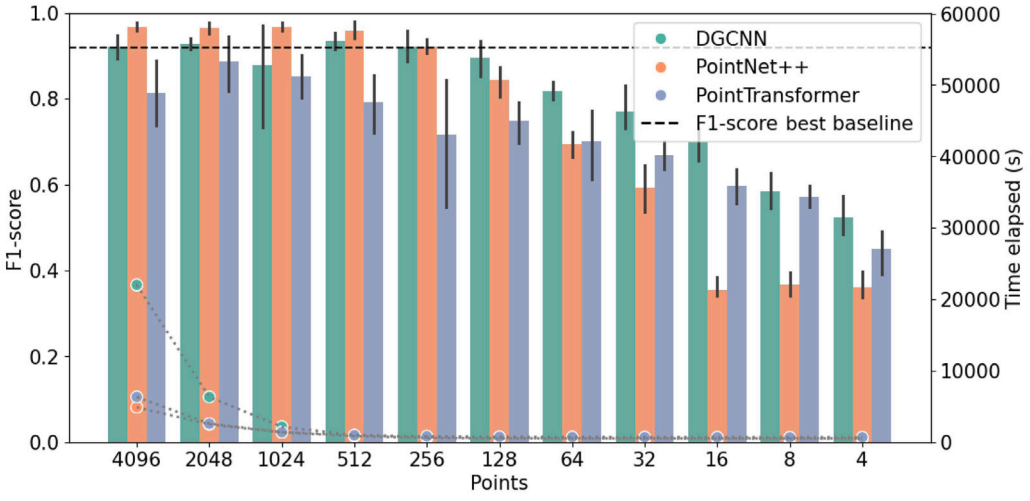

Fig. 6. F1-score mean and standard deviation (bars and vertical line) and time in seconds (points) for Analysis II: Individual disease separability, focused on PD. F1-score for the best configuration 0.97 ± 0.01, and for the best CNN baseline 0.92 ± 0.05.

4. Discussion

In the results of Analysis I, configurations as little as 512 points achieve top-performing metrics by only doubling the times of the smaller possible setting with 4 points. In terms of F1-score, PointNet++ with this medium size achieved a 0.92 ± 0.05, while the best metric is at with a 0.95 ± 0.02 with 4096 points. Regarding DGCNN, it showed a behaviour approximately 5% worse at most, while PointTransformer performance was 2% to 10% worse. Hence, despite the differences between architectures, patterns of neurodegenerative affectation can be seen in point clouds without the need of large amounts of data if a suitable architecture is used, in this case PointNet++.

Table 2
Test results for Analysis II: Individual disease separability, focused on AD.

Input size	Architecture	Accuracy	Precision	Recall	F1-score	AUROC
3*6,348,800 pixels	SEResNet152	0.86 ± 0.03	0.58 ± 0.17	0.33 ± 0.12	0.42 ± 0.14	0.89 ± 0.03
	EfficientNet	0.85 ± 0.04	0.75 ± 0.35	0.23 ± 0.09	0.33 ± 0.11	0.64 ± 0.13
	3D DenseNet161	0.90 ± 0.03	1.00 ± 0.00	0.37 ± 0.18	0.51 ± 0.21	0.93 ± 0.09
3*4,096 3D points	DGCNN	0.79 ± 0.21	0.79 ± 0.19	0.79 ± 0.21	0.75 ± 0.19	0.97 ± 0.04
	PointNet++	0.91 ± 0.05	0.89 ± 0.08	0.91 ± 0.05	0.90 ± 0.06	0.98 ± 0.03
	PointTransformer	0.78 ± 0.11	0.92 ± 0.05	0.78 ± 0.11	0.81 ± 0.11	0.97 ± 0.05
3*2,048 3D points	DGCNN	0.91 ± 0.06	0.93 ± 0.05	0.91 ± 0.06	0.92 ± 0.05	0.97 ± 0.03
	PointNet++	0.91 ± 0.05	0.94 ± 0.06	0.91 ± 0.05	0.92 ± 0.05	0.94 ± 0.05
	PointTransformer	0.89 ± 0.12	0.90 ± 0.07	0.89 ± 0.12	0.87 ± 0.10	0.97 ± 0.04
3*1,024 3D points	DGCNN	0.87 ± 0.13	0.83 ± 0.15	0.87 ± 0.13	0.80 ± 0.22	0.95 ± 0.06
	PointNet++	0.93 ± 0.05	0.92 ± 0.07	0.93 ± 0.05	0.93 ± 0.06	0.96 ± 0.06
	PointTransformer	0.84 ± 0.15	0.82 ± 0.11	0.84 ± 0.15	0.77 ± 0.14	0.99 ± 0.01
3*512 3D points	DGCNN	0.89 ± 0.07	0.93 ± 0.06	0.89 ± 0.07	0.91 ± 0.06	0.95 ± 0.06
	PointNet++	0.93 ± 0.07	0.88 ± 0.07	0.93 ± 0.07	0.90 ± 0.06	0.93 ± 0.09
	PointTransformer	0.77 ± 0.16	0.62 ± 0.30	0.77 ± 0.16	0.62 ± 0.29	0.95 ± 0.03
3*256 3D points	DGCNN	0.86 ± 0.11	0.83 ± 0.17	0.86 ± 0.11	0.81 ± 0.17	0.95 ± 0.06
	PointNet++	0.89 ± 0.06	0.88 ± 0.08	0.89 ± 0.06	0.87 ± 0.04	0.94 ± 0.05
	PointTransformer	0.78 ± 0.06	0.76 ± 0.13	0.78 ± 0.06	0.72 ± 0.11	0.91 ± 0.06
3*128 3D points	DGCNN	0.85 ± 0.06	0.76 ± 0.08	0.85 ± 0.06	0.77 ± 0.08	0.94 ± 0.05
	PointNet++	0.87 ± 0.09	0.75 ± 0.07	0.87 ± 0.09	0.78 ± 0.08	0.92 ± 0.06
	PointTransformer	0.70 ± 0.08	0.68 ± 0.09	0.70 ± 0.08	0.62 ± 0.15	0.83 ± 0.08
3*64 3D points	DGCNN	0.81 ± 0.08	0.73 ± 0.08	0.81 ± 0.08	0.72 ± 0.13	0.90 ± 0.05
	PointNet++	0.67 ± 0.06	0.60 ± 0.03	0.67 ± 0.06	0.56 ± 0.06	0.70 ± 0.10
	PointTransformer	0.66 ± 0.10	0.62 ± 0.05	0.66 ± 0.10	0.52 ± 0.19	0.79 ± 0.05
3*32 3D points	DGCNN	0.77 ± 0.09	0.74 ± 0.12	0.77 ± 0.09	0.70 ± 0.08	0.86 ± 0.05
	PointNet++	0.55 ± 0.12	0.54 ± 0.07	0.55 ± 0.12	0.48 ± 0.12	0.60 ± 0.08
	PointTransformer	0.65 ± 0.06	0.67 ± 0.07	0.65 ± 0.06	0.54 ± 0.17	0.80 ± 0.06
3*16 3D points	DGCNN	0.60 ± 0.14	0.56 ± 0.08	0.60 ± 0.14	0.52 ± 0.11	0.68 ± 0.12
	PointNet++	0.51 ± 0.06	0.50 ± 0.04	0.51 ± 0.06	0.42 ± 0.07	0.49 ± 0.04
	PointTransformer	0.61 ± 0.07	0.56 ± 0.03	0.61 ± 0.07	0.53 ± 0.05	0.64 ± 0.08
3*8 3D points	DGCNN	0.62 ± 0.09	0.58 ± 0.06	0.62 ± 0.09	0.56 ± 0.07	0.66 ± 0.10
	PointNet++	0.51 ± 0.08	0.34 ± 0.22	0.51 ± 0.08	0.30 ± 0.14	0.58 ± 0.09
	PointTransformer	0.59 ± 0.09	0.55 ± 0.05	0.59 ± 0.09	0.54 ± 0.06	0.63 ± 0.13
3*4 3D points	DGCNN	0.52 ± 0.07	0.52 ± 0.05	0.52 ± 0.07	0.40 ± 0.09	0.61 ± 0.14
	PointNet++	0.49 ± 0.02	0.33 ± 0.20	0.49 ± 0.02	0.31 ± 0.14	0.47 ± 0.11
	PointTransformer	0.56 ± 0.09	0.54 ± 0.06	0.56 ± 0.09	0.51 ± 0.08	0.63 ± 0.04

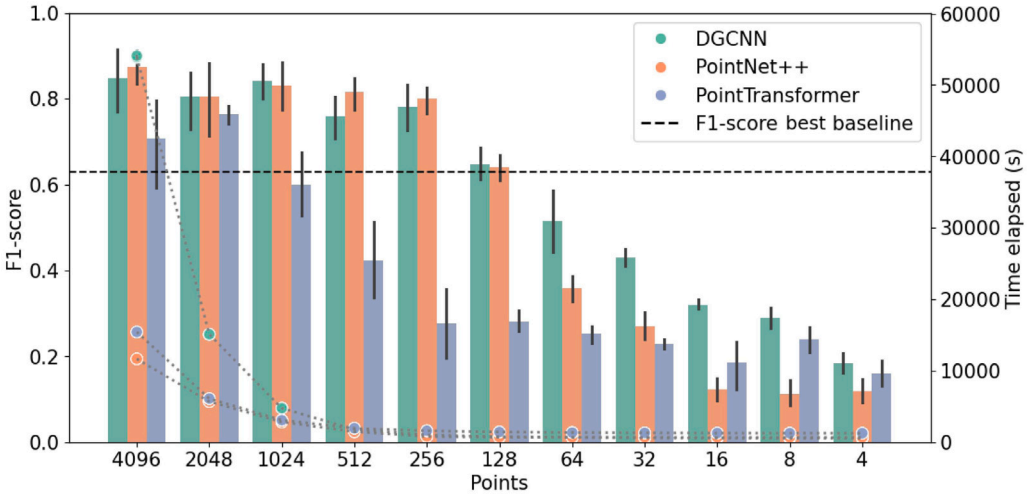

Fig. 7. F1-score mean and standard deviation (bars and vertical line) and time in seconds (points) for Analysis III: All classes separability. F1-score for the best configuration 0.87 ± 0.05, and for the best CNN baseline 0.63 ± 0.05.

Analysis II produced good results for AD, MS, and PD with configurations of PointNet++ of 1024, 4096, and 1024 points, respectively. In particular, each obtained F1-score values of 0.93 ± 0.06, 0.94 ± 0.02, and 0.97 ± 0.01. This reinforces the previous idea of NDD patterns being present even in simplified point clouds.

In Analysis III, the all versus all screening obtained a 0.87 ± 0.05. Metrics kept improving with the addition of points, although the improvement is marginal from 512 on. This analysis poses a task much complex than the previous cases, but the aforementioned characteristics of each disease are unique enough to provide features for the archi-

Table 3
Test results for Analysis II: Individual disease separability, focused on MS.

Input size	Architecture	Accuracy	Precision	Recall	F1-score	AUROC
3*6,348,800 pixels	SEResNet152	0.76 ± 0.03	0.79 ± 0.05	0.93 ± 0.06	0.85 ± 0.01	0.78 ± 0.04
	EfficientNet	0.73 ± 0.02	0.76 ± 0.01	0.92 ± 0.04	0.83 ± 0.02	0.73 ± 0.02
	3D DenseNet161	0.91 ± 0.03	0.96 ± 0.03	0.91 ± 0.04	0.94 ± 0.02	0.97 ± 0.02
3*4,096 3D points	DGCNN	0.91 ± 0.05	0.92 ± 0.01	0.91 ± 0.05	0.91 ± 0.03	0.98 ± 0.01
	PointNet++	0.95 ± 0.01	0.93 ± 0.03	0.95 ± 0.01	0.94 ± 0.02	0.99 ± 0.01
	PointTransformer	0.84 ± 0.11	0.90 ± 0.05	0.84 ± 0.11	0.84 ± 0.09	0.98 ± 0.01
3*2,048 3D points	DGCNN	0.90 ± 0.03	0.84 ± 0.05	0.90 ± 0.03	0.85 ± 0.06	0.97 ± 0.01
	PointNet++	0.95 ± 0.01	0.91 ± 0.02	0.95 ± 0.01	0.93 ± 0.02	0.99 ± 0.01
	PointTransformer	0.89 ± 0.05	0.88 ± 0.01	0.89 ± 0.05	0.88 ± 0.03	0.96 ± 0.01
3*1,024 3D points	DGCNN	0.87 ± 0.05	0.84 ± 0.06	0.87 ± 0.05	0.84 ± 0.06	0.98 ± 0.01
	PointNet++	0.94 ± 0.02	0.92 ± 0.03	0.94 ± 0.02	0.93 ± 0.02	0.98 ± 0.01
	PointTransformer	0.82 ± 0.07	0.77 ± 0.06	0.82 ± 0.07	0.74 ± 0.10	0.95 ± 0.02
3*512 3D points	DGCNN	0.89 ± 0.03	0.86 ± 0.06	0.89 ± 0.03	0.86 ± 0.06	0.96 ± 0.01
	PointNet++	0.92 ± 0.05	0.90 ± 0.04	0.92 ± 0.05	0.90 ± 0.04	0.98 ± 0.02
	PointTransformer	0.81 ± 0.10	0.84 ± 0.04	0.81 ± 0.10	0.79 ± 0.10	0.92 ± 0.02
3*256 3D points	DGCNN	0.88 ± 0.05	0.86 ± 0.05	0.88 ± 0.05	0.86 ± 0.05	0.96 ± 0.01
	PointNet++	0.89 ± 0.02	0.83 ± 0.02	0.89 ± 0.02	0.85 ± 0.02	0.96 ± 0.01
	PointTransformer	0.73 ± 0.08	0.73 ± 0.03	0.73 ± 0.08	0.67 ± 0.08	0.89 ± 0.01
3*128 3D points	DGCNN	0.84 ± 0.03	0.78 ± 0.04	0.84 ± 0.03	0.78 ± 0.05	0.93 ± 0.02
	PointNet++	0.80 ± 0.03	0.75 ± 0.03	0.80 ± 0.03	0.76 ± 0.03	0.89 ± 0.03
	PointTransformer	0.76 ± 0.01	0.71 ± 0.01	0.76 ± 0.01	0.66 ± 0.02	0.87 ± 0.02
3*64 3D points	DGCNN	0.78 ± 0.02	0.72 ± 0.02	0.78 ± 0.02	0.71 ± 0.03	0.87 ± 0.02
	PointNet++	0.68 ± 0.02	0.65 ± 0.02	0.68 ± 0.02	0.59 ± 0.03	0.78 ± 0.02
	PointTransformer	0.73 ± 0.04	0.69 ± 0.02	0.73 ± 0.04	0.61 ± 0.06	0.85 ± 0.03
3*32 3D points	DGCNN	0.76 ± 0.02	0.71 ± 0.02	0.76 ± 0.02	0.69 ± 0.04	0.84 ± 0.02
	PointNet++	0.63 ± 0.04	0.61 ± 0.03	0.63 ± 0.04	0.55 ± 0.04	0.68 ± 0.03
	PointTransformer	0.71 ± 0.04	0.68 ± 0.03	0.71 ± 0.04	0.65 ± 0.05	0.79 ± 0.02
3*16 3D points	DGCNN	0.67 ± 0.05	0.64 ± 0.04	0.67 ± 0.05	0.62 ± 0.04	0.75 ± 0.06
	PointNet++	0.51 ± 0.03	0.53 ± 0.08	0.51 ± 0.03	0.30 ± 0.04	0.54 ± 0.05
	PointTransformer	0.65 ± 0.04	0.62 ± 0.03	0.65 ± 0.04	0.61 ± 0.05	0.72 ± 0.03
3*8 3D points	DGCNN	0.61 ± 0.03	0.59 ± 0.03	0.61 ± 0.03	0.52 ± 0.03	0.67 ± 0.01
	PointNet++	0.50 ± 0.01	0.29 ± 0.20	0.50 ± 0.01	0.24 ± 0.04	0.55 ± 0.06
	PointTransformer	0.59 ± 0.05	0.54 ± 0.09	0.59 ± 0.05	0.52 ± 0.05	0.62 ± 0.09
3*4 3D points	DGCNN	0.56 ± 0.02	0.56 ± 0.02	0.56 ± 0.02	0.44 ± 0.04	0.61 ± 0.05
	PointNet++	0.50 ± 0.00	0.27 ± 0.17	0.50 ± 0.00	0.23 ± 0.02	0.50 ± 0.04
	PointTransformer	0.56 ± 0.04	0.61 ± 0.03	0.56 ± 0.04	0.35 ± 0.09	0.58 ± 0.06

tectures to distinguish them effectively. Thus, these are simple enough to be condensed in a greatly smaller subset of points that also keeps each disease individual characteristics that makes it differentiable from others that might share some morphological patterns.

Since each disease has its own nuances, Fig. 8 summarizes the F1-score for each class when considered individually, i.e Analysis II and III. Analysis II shows that the class with a superior performance across most point configurations is PD, which is surprising giving that is not the most populated class. That would be MS, that performs slightly under until 512 points are reached. PD patients could present retinal layers dispositions easily captured with less points and more consistently present in all cases, while our MS cohort is more heterogeneous in terms of retinal layer affectations which leads to needing more complex graphs to fully capture all of its differences. Another reason could be the localization of these changes, as random unlocalized subsampling could benefit some patterns dispositions. In this sense, AD shows a similar MS behaviour, albeit more unstable. The reason for this might be more related to the small amount of samples in comparison with the others. Regarding Analysis III presents PD and MS classes closer and AD further, which correlates with classes being compared at the same time, a situation where the most frequent ones would have some advantage. In both analysis, stabilization in the metrics for most architectures is seen at 256 points. Improvement in this sense could come from the addition and balancing of more samples.

Regarding the differences between the GDL architectures used, when the granularity of the point clouds decreases, DGCNN performs better than PointNet++, albeit not satisfactorily enough. This opposite behaviour might indicate the dynamic graph approach of DGCNN thrives in smaller point clouds, where the hierarchical feature learning of PointNet++ benefits from larger data. In every situation, PointTransformer shows the worst results, which suggests a transformer-based approach does not capture well this type of data. Additionally, since the point clouds were randomly subsampled, these architectures might also benefit from larger data. In any case, PointNet++ top performance is similar or better than a 3D CNN and typically only needs around 8% of the total points of the sample. This proves how much data efficient is using GDL with respect to traditional methods.

In terms of comparisons, our results outperform the proposed baselines. Although the best baseline, DenseNet, is a competitive model, the results show the benefits in terms of classification metrics when transforming segmentation masks into point clouds where potential redundant points are eliminated. However, comparison with the state-of-the-art is not possible as there is no open dataset or methods to do so.

Regarding hardware resource usage, we measured the average time required for training and inference across both the baseline and GDL methods. For training, the baselines EfficientNet, SEResNet, and DenseNet took 43, 131, and 146 min per fold, respectively. Among the GDL approaches, we focused on the best-performing point configurations (starting from 1024 points), observing that DGCNN required 56, 174, and 618 min; PointNet++ took 34, 67, and 134 min; and PointTransformer needed 36, 71, and 177 min per fold. In terms of inference time per sample, the baselines took 9.54 (EfficientNet), 11.69 (SEResNet), and 10.18 (DenseNet) seconds. In contrast, GDL models were notably faster: DGCNN needed 2.33, 3.97, and 7.01 s; PointNet++ took 0.63, 0.66, and 2.22 s; and PointTransformer required 1.89, 2.47,

Table 4
Test results for Analysis II: Individual disease separability, focused on PD.

Input size	Architecture	Accuracy	Precision	Recall	F1-score	AUROC
3*6,348,800 pixels	SEResNet152	0.73 ± 0.02	0.75 ± 0.07	0.68 ± 0.16	0.70 ± 0.06	0.81 ± 0.05
	EfficientNet	0.67 ± 0.04	0.66 ± 0.09	0.75 ± 0.2	0.68 ± 0.08	0.77 ± 0.04
	3D DenseNet161	0.92 ± 0.06	0.91 ± 0.10	0.94 ± 0.06	0.92 ± 0.05	0.99 ± 0.01
3*4,096 3D points	DGCNN	0.92 ± 0.03	0.93 ± 0.03	0.92 ± 0.03	0.92 ± 0.03	0.98 ± 0.01
	PointNet++	0.97 ± 0.01	0.97 ± 0.01	0.97 ± 0.01	0.97 ± 0.01	0.98 ± 0.01
	PointTransformer	0.82 ± 0.08	0.88 ± 0.04	0.82 ± 0.08	0.81 ± 0.09	0.98 ± 0.01
3*2,048 3D points	DGCNN	0.93 ± 0.02	0.94 ± 0.02	0.93 ± 0.02	0.93 ± 0.02	0.98 ± 0.01
	PointNet++	0.96 ± 0.02	0.96 ± 0.02	0.96 ± 0.02	0.96 ± 0.02	0.97 ± 0.01
	PointTransformer	0.89 ± 0.07	0.91 ± 0.04	0.89 ± 0.07	0.89 ± 0.07	0.96 ± 0.02
3*1,024 3D points	DGCNN	0.89 ± 0.12	0.92 ± 0.07	0.89 ± 0.12	0.88 ± 0.14	0.98 ± 0.01
	PointNet++	0.97 ± 0.01	0.97 ± 0.01	0.97 ± 0.01	0.97 ± 0.01	0.99 ± 0.01
	PointTransformer	0.86 ± 0.06	0.89 ± 0.03	0.86 ± 0.06	0.85 ± 0.06	0.97 ± 0.01
3*512 3D points	DGCNN	0.94 ± 0.02	0.94 ± 0.02	0.94 ± 0.02	0.94 ± 0.02	0.98 ± 0.01
	PointNet++	0.96 ± 0.02	0.96 ± 0.02	0.96 ± 0.02	0.96 ± 0.02	0.99 ± 0.01
	PointTransformer	0.80 ± 0.07	0.83 ± 0.04	0.80 ± 0.07	0.79 ± 0.08	0.94 ± 0.02
3*256 3D points	DGCNN	0.92 ± 0.04	0.93 ± 0.04	0.92 ± 0.04	0.92 ± 0.04	0.97 ± 0.01
	PointNet++	0.92 ± 0.02	0.93 ± 0.02	0.92 ± 0.02	0.92 ± 0.02	0.97 ± 0.01
	PointTransformer	0.75 ± 0.12	0.82 ± 0.06	0.75 ± 0.12	0.71 ± 0.17	0.90 ± 0.04
3*128 3D points	DGCNN	0.90 ± 0.05	0.91 ± 0.04	0.90 ± 0.05	0.90 ± 0.05	0.96 ± 0.02
	PointNet++	0.84 ± 0.04	0.85 ± 0.04	0.84 ± 0.04	0.84 ± 0.04	0.94 ± 0.02
	PointTransformer	0.75 ± 0.05	0.77 ± 0.04	0.75 ± 0.05	0.75 ± 0.05	0.87 ± 0.03
3*64 3D points	DGCNN	0.82 ± 0.02	0.83 ± 0.03	0.82 ± 0.02	0.82 ± 0.02	0.90 ± 0.03
	PointNet++	0.70 ± 0.03	0.71 ± 0.04	0.70 ± 0.03	0.69 ± 0.03	0.78 ± 0.04
	PointTransformer	0.72 ± 0.07	0.77 ± 0.03	0.72 ± 0.07	0.70 ± 0.09	0.86 ± 0.04
3*32 3D points	DGCNN	0.78 ± 0.06	0.81 ± 0.04	0.78 ± 0.06	0.77 ± 0.06	0.86 ± 0.05
	PointNet++	0.61 ± 0.05	0.63 ± 0.05	0.61 ± 0.05	0.59 ± 0.06	0.65 ± 0.03
	PointTransformer	0.68 ± 0.03	0.70 ± 0.03	0.68 ± 0.03	0.67 ± 0.04	0.77 ± 0.04
3*16 3D points	DGCNN	0.71 ± 0.04	0.73 ± 0.04	0.71 ± 0.04	0.70 ± 0.04	0.80 ± 0.04
	PointNet++	0.50 ± 0.00	0.31 ± 0.10	0.50 ± 0.00	0.35 ± 0.03	0.51 ± 0.07
	PointTransformer	0.63 ± 0.03	0.71 ± 0.05	0.63 ± 0.03	0.60 ± 0.05	0.77 ± 0.05
3*8 3D points	DGCNN	0.61 ± 0.03	0.67 ± 0.03	0.61 ± 0.03	0.58 ± 0.05	0.68 ± 0.06
	PointNet++	0.49 ± 0.04	0.36 ± 0.15	0.49 ± 0.04	0.37 ± 0.04	0.50 ± 0.11
	PointTransformer	0.60 ± 0.03	0.66 ± 0.06	0.60 ± 0.03	0.57 ± 0.03	0.66 ± 0.07
3*4 3D points	DGCNN	0.57 ± 0.04	0.64 ± 0.07	0.57 ± 0.04	0.52 ± 0.05	0.62 ± 0.05
	PointNet++	0.49 ± 0.01	0.34 ± 0.11	0.49 ± 0.01	0.36 ± 0.04	0.48 ± 0.07
	PointTransformer	0.55 ± 0.03	0.62 ± 0.19	0.55 ± 0.03	0.45 ± 0.06	0.61 ± 0.03

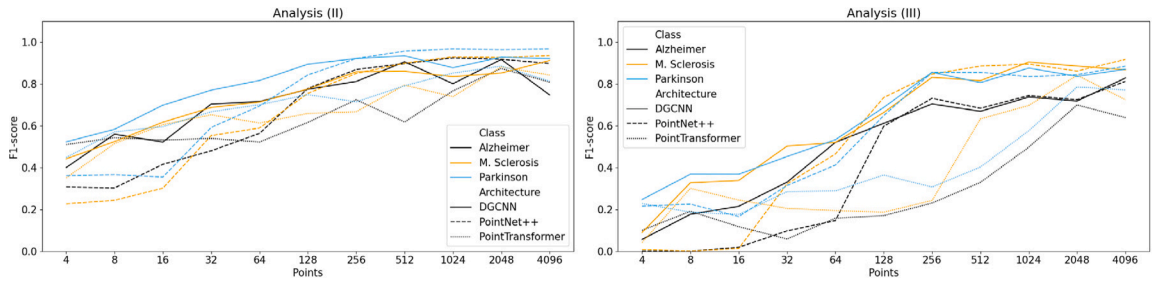

Fig. 8. F1-score class-wise results summary for Analysis II (left) and III (right).

and 4.41 s. Fig. 9 illustrates the peak memory usage recorded during training and inference for each method. Overall, GDL methods tend to require longer training times due to their architectural complexity. However, their lower input data footprint translates into faster inference and significantly reduced memory consumption during both training and evaluation. It is also important to note that these metrics provide a general overview of resource usage and are influenced by several factors, including batch size, hardware specifications, software libraries, and implementation-level optimizations.

Regarding the clinical relevance, firstly, since point clouds can hold significant information to discern pathological and control individuals, a new way of researching biomarkers is raised instead of 2D masks with retinal layer thickness, which could lead to new disease-related patterns. Secondly, GDL as a screening method showed powerful results for NDDs, which could impulse the creation of computer-aided applications that guide the difficult diagnosis of these pathologies. Besides, these techniques have the potential to have a smaller computational load as they use less data points, which positively impacts temporal efficiency providing faster and more accurate diagnosis. Finally, the lack of reliable neurophthalmological biomarkers can be alleviated by strong computational means to impulse and diversify their research, like GDL.

5. Conclusions

In this work new GDL approaches have been successfully applied, improving the current state of the art classification metrics for MS and reporting the first for AD and PD. Three different analysis were conducted to study the separability of each class against a control group, as well as the impact of the granularity of the data. This is the first work to perform NDD pathological screening with GDL methods considering several diseases at the same time.

Table 5
Test results for Analysis III: All classes separability.

Input size	Architecture	Accuracy	Precision	Recall	F1-score	AUROC
3*6,348,800 pixels	SEResNet152	0.47 ± 0.03	0.54 ± 0.06	0.47 ± 0.03	0.48 ± 0.03	0.78 ± 0.03
	EfficientNet	0.39 ± 0.04	0.44 ± 0.05	0.39 ± 0.04	0.39 ± 0.04	0.69 ± 0.01
	3D DenseNet161	0.65 ± 0.05	0.63 ± 0.05	0.65 ± 0.05	0.63 ± 0.05	0.94 ± 0.03
3*4,096 3D points	DGCNN	0.86 ± 0.06	0.86 ± 0.08	0.86 ± 0.06	0.85 ± 0.08	0.97 ± 0.02
	PointNet++	0.89 ± 0.05	0.86 ± 0.05	0.89 ± 0.05	0.87 ± 0.05	0.97 ± 0.01
	PointTransformer	0.77 ± 0.09	0.73 ± 0.07	0.77 ± 0.09	0.71 ± 0.11	0.93 ± 0.03
3*2,048 3D points	DGCNN	0.84 ± 0.03	0.81 ± 0.09	0.84 ± 0.03	0.80 ± 0.08	0.96 ± 0.02
	PointNet++	0.83 ± 0.08	0.80 ± 0.10	0.83 ± 0.08	0.80 ± 0.10	0.96 ± 0.03
	PointTransformer	0.81 ± 0.03	0.75 ± 0.03	0.81 ± 0.03	0.76 ± 0.02	0.93 ± 0.02
3*1,024 3D points	DGCNN	0.87 ± 0.05	0.84 ± 0.05	0.87 ± 0.05	0.84 ± 0.05	0.97 ± 0.02
	PointNet++	0.87 ± 0.05	0.82 ± 0.07	0.87 ± 0.05	0.83 ± 0.07	0.97 ± 0.02
	PointTransformer	0.66 ± 0.09	0.66 ± 0.10	0.66 ± 0.09	0.60 ± 0.09	0.89 ± 0.04
3*512 3D points	DGCNN	0.82 ± 0.03	0.75 ± 0.06	0.82 ± 0.03	0.76 ± 0.06	0.96 ± 0.01
	PointNet++	0.86 ± 0.04	0.79 ± 0.03	0.86 ± 0.04	0.81 ± 0.04	0.97 ± 0.01
	PointTransformer	0.50 ± 0.10	0.45 ± 0.12	0.50 ± 0.10	0.42 ± 0.10	0.79 ± 0.07
3*256 3D points	DGCNN	0.84 ± 0.05	0.77 ± 0.07	0.84 ± 0.05	0.78 ± 0.07	0.96 ± 0.02
	PointNet++	0.84 ± 0.04	0.78 ± 0.04	0.84 ± 0.04	0.80 ± 0.03	0.96 ± 0.01
	PointTransformer	0.44 ± 0.07	0.40 ± 0.06	0.44 ± 0.07	0.28 ± 0.09	0.69 ± 0.06
3*128 3D points	DGCNN	0.75 ± 0.03	0.63 ± 0.05	0.75 ± 0.03	0.65 ± 0.04	0.91 ± 0.02
	PointNet++	0.72 ± 0.05	0.62 ± 0.03	0.72 ± 0.05	0.64 ± 0.03	0.89 ± 0.02
	PointTransformer	0.41 ± 0.03	0.42 ± 0.05	0.41 ± 0.03	0.28 ± 0.03	0.67 ± 0.03
3*64 3D points	DGCNN	0.62 ± 0.07	0.54 ± 0.08	0.62 ± 0.07	0.51 ± 0.09	0.83 ± 0.03
	PointNet++	0.44 ± 0.03	0.40 ± 0.03	0.44 ± 0.03	0.36 ± 0.03	0.70 ± 0.02
	PointTransformer	0.38 ± 0.03	0.39 ± 0.02	0.38 ± 0.03	0.25 ± 0.02	0.62 ± 0.02
3*32 3D points	DGCNN	0.58 ± 0.03	0.44 ± 0.02	0.58 ± 0.03	0.43 ± 0.02	0.77 ± 0.01
	PointNet++	0.35 ± 0.05	0.35 ± 0.02	0.35 ± 0.05	0.27 ± 0.04	0.60 ± 0.02
	PointTransformer	0.33 ± 0.03	0.37 ± 0.01	0.33 ± 0.03	0.23 ± 0.01	0.60 ± 0.03
3*16 3D points	DGCNN	0.45 ± 0.04	0.36 ± 0.01	0.45 ± 0.04	0.32 ± 0.01	0.67 ± 0.02
	PointNet++	0.25 ± 0.00	0.14 ± 0.11	0.25 ± 0.00	0.12 ± 0.03	0.51 ± 0.03
	PointTransformer	0.33 ± 0.04	0.31 ± 0.05	0.33 ± 0.04	0.19 ± 0.06	0.58 ± 0.04
3*8 3D points	DGCNN	0.38 ± 0.03	0.36 ± 0.04	0.38 ± 0.03	0.29 ± 0.03	0.59 ± 0.01
	PointNet++	0.26 ± 0.03	0.08 ± 0.03	0.26 ± 0.03	0.11 ± 0.04	0.52 ± 0.04
	PointTransformer	0.35 ± 0.05	0.32 ± 0.07	0.35 ± 0.05	0.24 ± 0.03	0.57 ± 0.04
3*4 3D points	DGCNN	0.29 ± 0.02	0.26 ± 0.10	0.29 ± 0.02	0.18 ± 0.03	0.56 ± 0.03
	PointNet++	0.27 ± 0.02	0.12 ± 0.06	0.27 ± 0.02	0.12 ± 0.03	0.50 ± 0.03
	PointTransformer	0.31 ± 0.02	0.18 ± 0.10	0.31 ± 0.02	0.16 ± 0.03	0.55 ± 0.03

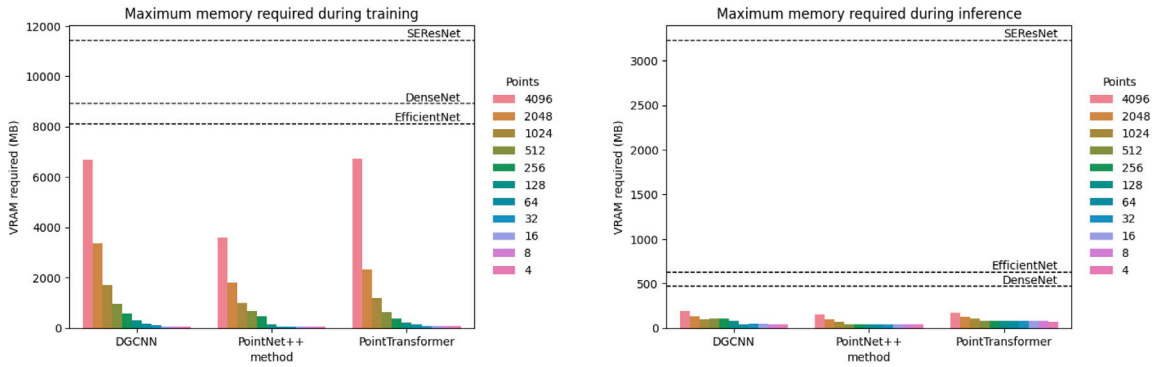

Fig. 9. Maximum memory required for baselines and GDL methods during training (left) and inference of a single sample (right).

The results of the three analysis offered satisfactory results for all the NDD considered: MS, AD, and PD. Our analysis successfully showed that randomly subsampled point clouds could hold the nuances that characterize each of the diseases, providing enough information to identify them against control groups or others similar diseases that might have similar morphological patterns. In this sense, PD showed signs of having more significant retinal layers dispositions captured by the point clouds than other diseases like MS, which despite of presenting more samples, did not achieve metrics as high as PD. Not only does this prove the potential of processing retinal layers data as point clouds in terms of screening ability and computational biomarkers extraction, but also in terms of efficiency as considered subsets are much smaller than its original sizes, decreasing its computational load.

As future work, further research could focus on refining the subsampled point clouds to better capture morphological differences between pathologies and define more precise computational biomarkers. Sector-based analysis may help localize the most relevant retinal regions, while including additional layers and evaluating them in a disease-specific manner could increase the overall discriminatory power. The framework may also be extended to other conditions that induce retinal morphological changes. Moreover, future directions include the evaluation of alternative preprocessing strategies, robustness testing under variable imaging conditions (e.g., noise or resolution changes), and

external validation using new datasets to enhance generalizability and clinical relevance.

CRediT authorship contribution statement

Lorena Álvarez-Rodríguez: Writing – review & editing, Visualization, Writing – original draft, Software, Data curation, Methodology. **Ana Pueyo:** Investigation, Data curation. **Joaquim de Moura:** Project administration, Writing – original draft, Supervision, Conceptualization, Writing – review & editing, Validation. **Iván García Prego:** Software, Data curation. **Elisa Vilades:** Supervision, Investigation, Validation, Project administration, Data curation. **Elena Garcia-Martin:** Validation, Project administration, Data curation, Supervision, Investigation. **Clara I. Sánchez:** Supervision, Investigation, Validation, Project administration, Data curation. **Jorge Novo:** Writing – review & editing, Validation, Project administration, Supervision, Conceptualization. **Marcos Ortega:** Project administration, Supervision, Funding acquisition, Writing – review & editing, Conceptualization.

Funding

This work was supported by the Instituto de Salud Carlos III, Spain (ISCIII), Government of Spain [grant numbers PI17/01726, PI20/00437, PI23/00935, RD21/0002/0050 (Inflammatory Disease Network - RICORS), FORT23/00010 (Programa FORTALECE)], the Ministerio de Ciencia e Innovación, Spain, Government of Spain [grant numbers PID2023-148913OB-I00, TED2021-131201B-I00, and PDC2022-133132-I00], the Consellería de Educación, Universidade, e Formación Profesional, Xunta de Galicia, Spain, Grupos de Referencia Competitiva [grant number ED431C 2024/33] and by the Government of Aragon [group B2323R]. This work was also supported by the Horizon Europe Programme through the ACHILLES/101189689 project (HORIZON-CL4-2024-DATA-01-01). Also supported by the CNPq/MCTI/FNDCT [grant Number: 444625/2024-0]. Funding for open access charge: Universidade da Coruña/CISUG.

Declaration of competing interest

The authors declare that they have no known competing financial interests or personal relationships that could have appeared to influence the work reported in this paper.

Data availability

The authors do not have permission to share data.

References

[1] L. Angelini, G. Paparella, M. Bologna, Distinguishing essential tremor from Parkinson's disease: clinical and experimental tools, Expert. Rev. Neurother. 24 (8) (2024) 799–814.

[2] J. Dumurgier, C. Tzourio, Epidemiology of neurological diseases in older adults, Rev. Neurol. 176 (9) (2020) 642–648.

[3] P. Song, Y. Zhang, M. Zha, Q. Yang, X. Ye, Q. Yi, I. Rudan, The global prevalence of essential tremor, with emphasis on age and sex: a meta-analysis, J. Glob. Heal. 11 (2021).

[4] G. Deuschl, E. Beghi, F. Fazekas, T. Varga, K.A. Christoforidi, E. Sipido, C.L. Bassetti, T. Vos, V.L. Feigin, The burden of neurological diseases in Europe: an analysis for the global burden of disease study 2017, Lancet Public Heal. 5 (10) (2020) e551–e567.

[5] E. Nichols, J.D. Steinmetz, S.E. Vollset, K. Fukutaki, J. Chalek, F. Abd-Allah, A. Abdoli, A. Abualhasan, E. Abu-Gharbieh, T.T. Akram, et al., Estimation of the global prevalence of dementia in 2019 and forecasted prevalence in 2050: an analysis for the global burden of disease study 2019, Lancet Public Heal. 7 (2) (2022) e105–e125.

[6] N. Grotewold, R.L. Albin, Update: Descriptive epidemiology of Parkinson disease, Parkinsonism Rel. Disord. (2024) 106000.

[7] C. Walton, R. King, L. Rechtman, W. Kaye, E. Leray, R.A. Marrie, N. Robertson, N. La Rocca, B. Uitdehaag, I. van Der Mei, et al., Rising prevalence of multiple sclerosis worldwide: Insights from the Atlas of MS, Mult. Scler. J. 26 (14) (2020) 1816–1821.

[8] M. Ptito, M. Bleau, J. Bouskila, The retina: a window into the brain, Cells 10 (12) (2021) 3269.

[9] I. López-Cuenca, A. Marcos-Dolado, M. Yus-Fuertes, E. Salobrar-García, L. Elvira-Hurtado, J.A. Fernández-Albarral, J.J. Salazar, A.I. Ramírez, L. Sánchez-Puebla, M.E. Fuentes-Ferrer, et al., The relationship between retinal layers and brain areas in asymptomatic first-degree relatives of sporadic forms of Alzheimer's disease: an exploratory analysis, Alzheimer's Res. Ther. 14 (1) (2022) 79.

[10] C. Rascunà, C.E. Cicero, C.G. Chisari, A. Russo, L. Giuliano, N. Castellino, C. Terravecchia, M. Grillo, A. Longo, T. Avitabile, et al., Retinal thickness and microvascular pathway in idiopathic rapid eye movement sleep behaviour disorder and Parkinson's disease, Parkinsonism Rel. Disord. 88 (2021) 40–45.

[11] S. Mohana Devi, I. Mahalaxmi, N.P. Aswathy, V. Dhivya, V. Balachandar, Does retina play a role in Parkinson's disease? Acta Neurol. Belg. 120 (2020) 257–265.

[12] S. Vujosevic, M.M. Parra, M.E. Hartnett, L. O'Toole, A. Nuzzi, C. Limoli, E. Villani, P. Nucci, Optical coherence tomography as retinal imaging biomarker of neuroinflammation/neurodegeneration in systemic disorders in adults and children, Eye 37 (2) (2023) 203–219.

[13] J.S. Xie, L. Donaldson, E. Margolin, The use of optical coherence tomography in neurology: a review, Brain 145 (12) (2022) 4160–4177.

[14] C. Lo, L.N. Vuong, J.A. Micieli, Recent advances and future directions on the use of optical coherence tomography in neuro-ophthalmology, Taiwan J. Ophthalmol. 11 (1) (2021) 3–15.

[15] H.J. Shin, F. Costello, Imaging the optic nerve with optical coherence tomography, Eye 38 (12) (2024) 2365–2379.

[16] L. Castro-Roger, V. Mallen, E.V. Palomar, B.C. Ciordia, M.J.V. Altabás, A. Tello, M.J. Rodrigo, M.S. Perié, L.A. Campo, I. Munuera, E. Garcia-Martin, Role of optical coherence tomography in diagnosis of Alzheimer's disease, Acta Ophthalmol. 100 (S275) (2022) http://dx.doi.org/10.1111/j.1755-3768.2022.0184.

[17] S. Vaz-Pereira, T. Morais-Sarmento, R. Esteves Marques, Optical coherence tomography features of neovascularization in proliferative diabetic retinopathy: a systematic review, Int. J. Retin. Vitr. 6 (2020) 1–12.

[18] M. Everett, S. Magazzeni, T. Schmoll, M. Kempe, Optical coherence tomography: From technology to applications in ophthalmology, Transl. Biophotonics 3 (1) (2021) e202000012.

[19] N. Eladawi, M. Elmogy, M. Ghazal, A.H. Mahmoud, H. Mahmoud, M.T. Alhalabi, A. Aboelfetouh, A. Riad, R. Keynton, S. Schaal, et al., Optical coherence tomography: A review, Diabetes Fundus OCT (2020) 191–221.

[20] B.P. Gaire, Y. Koronyo, D.-T. Fuchs, H. Shi, A. Rentsendorj, R. Danziger, J.-P. Vit, N. Mirzaei, J. Doustar, J. Sheyn, et al., Alzheimer's disease pathophysiology in the retina, Prog. Retin. Eye Res. 101 (2024) 101273.

[21] S. Karatzetzou, D. Parisis, S. Ioannidis, T. Afrantou, P. Ioannidis, Optical coherence tomography as a biomarker in the differential diagnosis between Parkinson's disease and atypical Parkinsonian syndromes: A narrative review, Appl. Sci. 14 (6) (2024) 2491.

[22] M. Ortiz, V. Mallen, L. Boquete, E.M. Sánchez-Morla, B. Cordón, E. Vilades, F.J. Dongil-Moreno, J.M. Miguel-Jiménez, E. Garcia-Martin, Diagnosis of multiple sclerosis using optical coherence tomography supported by artificial intelligence, Mult. Scler. Relat. Disord. 74 (2023) 104725, http://dx.doi.org/10.1016/j.msard.2023.104725.

[23] S. Poveda, X. Arellano, O. Bernal-Pacheco, A. Valencia López, Structural changes in the retina as a potential biomarker in Parkinson's disease: an approach from optical coherence tomography, Front. Neuroimaging 3 (2024) 1340754.

[24] A. Tulsani, J. Patel, P. Kumar, V. Mayya, K. Pavithra, M. Geetha, S.V. Bhandary, S. Pathan, A novel convolutional neural network for identification of retinal layers using sliced optical coherence tomography images, Heal. Anal. 5 (2024) 100289.

[25] M. Gende, V. Mallen, J. de Moura, B. Cordón, E. Garcia-Martin, C.I. Sánchez, J. Novo, M. Ortega, Automatic segmentation of retinal layers in multiple neurodegenerative disorder scenarios, IEEE J. Biomed. Heal. Inform. (2023).

[26] Y. Turkan, F.B. Tek, F. Arpaci, O. Arslan, D. Toslak, M. Bulut, A. Yaman, Automated diagnosis of Alzheimer's disease using OCT and OCTA: A systematic review, IEEE Access (2024).

[27] F. Huang, A. Qiu, A.D.N. Initiative, et al., Ensemble vision transformer for dementia diagnosis, IEEE J. Biomed. Heal. Inform. (2024).

[28] Z. Khodabandeh, H. Rabbani, N. Shirani Bidabadi, M. Bonyani, R. Kafieh, Comprehensive Evaluation of Artificial Intelligence Models for Diagnosis of Multiple Sclerosis Using Information from Retinal Layers Multicenter OCT Images, Cold Spring Harbor Laboratory Press, 2024, pp. 2003–2024, MedRxiv.

[29] H. Fu, Y. Zhao, P.-T. Yap, C.-B. Schönlieb, A.F. Frangi, Guest editorial special issue on geometric deep learning in medical imaging, IEEE Trans. Med. Imaging 42 (2) (2023) 332–335.

[30] K.M. Timmins, I.C. Van der Schaaf, I.N. Vos, Y.M. Ruigrok, B.K. Velthuis, H.J. Kuijf, Geometric deep learning using vascular surface meshes for modality-independent unruptured intracranial aneurysm detection, IEEE Trans. Med. Imaging 42 (11) (2023) 3451–3460.

[31] Z. Huang, H. Cai, T. Dan, Y. Lin, P. Laurienti, G. Wu, Detecting brain state changes by geometric deep learning of functional dynamics on Riemannian manifold, in: Medical Image Computing and Computer Assisted Intervention–MICCAI 2021: 24th International Conference, Strasbourg, France, September 27–October 1, 2021, Proceedings, Part VII 24, Springer, 2021, pp. 543–552.
[32] R. Ghosh, K. Wong, Y.J. Zhang, G.W. Britz, S.T. Wong, Automated catheter segmentation and tip detection in cerebral angiography with topology-aware geometric deep learning, J. NeuroIntervent. Surg. 16 (3) (2024) 290–295.
[33] A.H. Thiéry, F. Braeu, T.A. Tun, T. Aung, M.J. Girard, Medical application of geometric deep learning for the diagnosis of Glaucoma, Transl. Vis. Sci. Technol. 12 (2) (2023) 23–23.
[34] L. Álvarez-Rodríguez, I.G. Prego, J. de Moura, A. Pueyo, E. Vilades, E. Garcia-Martin, C.I. Sánchez, J. Novo, M. Ortega, 3D point cloud analysis via transformer-based graph learning for multiple sclerosis screening in OCT images, 246, Elsevier BV, 2024, pp. 1080–1089, http://dx.doi.org/10.1016/j.procs.2024.09.527,
[35] L. Álvarez-Rodríguez, A. Pueyo, J. de Moura, E. Vilades, E. Garcia-Martin, C.I. Sánchez, J. Novo, M. Ortega, Fully automatic deep convolutional approaches for the screening of neurodegenerative diseases using multi-view OCT images, Artif. Intell. Med. 158 (2024) 103006, http://dx.doi.org/10.1016/j.artmed.2024.103006.
[36] F. Isensee, P.F. Jaeger, S.A.A. Kohl, J. Petersen, K.H. Maier-Hein, Nnu-net: a self-configuring method for deep learning-based biomedical image segmentation, Nature Methods 18 (2) (2020) 203–211, http://dx.doi.org/10.1038/s41592-020-01008-z.
[37] S.A. Taufik, N. Ramli, A.H. Tan, S.-Y. Lim, M.T.A. Ghani, N. Shahrizaila, Longitudinal changes in the retinal nerve fiber layer thickness in amyotrophic lateral sclerosis and Parkinson's disease, J. Clin. Neurol. (Seoul, Korea) 20 (3) (2024) 285.
[38] S. Toscano, C.G. Chisari, A. Biondi, F. Patti, Early reduction of retinal thickness predicts physical and cognitive disability in newly diagnosed multiple sclerosis patients: results from a cross-sectional study, Neurol. Sci. (2024) 1–10.
[39] L. Sánchez-Puebla, R. de Hoz, E. Salobrar-García, A. Arias-Vázquez, M. González-Jiménez, A.I. Ramírez, J.A. Fernández-Albarral, J.A. Matamoros, L. Elvira-Hurtado, T.C. Saido, et al., Age-related retinal layer thickness changes measured by OCT in APPNL-F/NL-F mice: Implications for Alzheimer's disease, Int. J. Mol. Sci. 25 (15) (2024) 8221.
[40] M. Singlas, T.-H.-C. Tran, W. Boucenna, M. Diouf, O. Godefroy, Is internal retinal thickness an early marker of Alzheimer's and Lewy body diseases? Rev. Neurol. 180 (3) (2024) 220–223.
[41] A. Camacho-Ordonez, A. Cervantes-Arriaga, M. Rodríguez-Violante, A.J. Hernandez-Medrano, S.A. Somilleda-Ventura, H.J. Pérez-Cano, Á. Nava-Castañeda, O. Guerrero-Berger, Is there any correlation between alpha-synuclein levels in tears and retinal layer thickness in Parkinson's disease? Eur. J. Ophthalmol. 34 (1) (2024) 252–259.
[42] B.C. Ciordia, M.J.V. Altabás, A. Tello, L. Castro-Roger, E.V. Palomar, M.J. Rodrigo, M.S. Perié, L.A. Campo, I. Munuera, M. Satue, E. Garcia-Martin, Evaluation of severity and time disease using new optical coherence tomography tool in multiple sclersosis patients, Acta Ophthalmol. 100 (S275) (2022) http://dx.doi.org/10.1111/j.1755-3768.2022.0074.
[43] C.R. Qi, L. Yi, H. Su, L.J. Guibas, PointNet++: Deep hierarchical feature learning on point sets in a metric space, 2017, arXiv preprint arXiv:1706.02413.
[44] Y. Wang, Y. Sun, Z. Liu, S.E. Sarma, M.M. Bronstein, J.M. Solomon, Dynamic graph CNN for learning on point clouds, ACM Trans. Graph. (2019).
[45] H. Zhao, L. Jiang, J. Jia, P.H. Torr, V. Koltun, Point transformer, in: Proceedings of the IEEE/CVF International Conference on Computer Vision, 2021, pp. 16259–16268.
[46] W. Wang, H. Zhou, Y. Yan, X. Cheng, P. Yang, L. Gan, S. Kuang, An automatic extraction method on medical feature points based on PointNet++ for robot-assisted knee arthroplasty, Int. J. Med. Robot. Comput. Assisted Surg. 19 (1) (2023) e2464.
[47] J. Yang, Z. Li, P. Zhan, X. Li, K. Wang, J. Han, P. Yang, Proximal femur parameter measurement via improved PointNet++, Int. J. Med. Robot. Comput. Assisted Surg. 19 (3) (2023) e2494.
[48] A. Fusco, M. Akkus, N. Vysotskaya, S. Hazra, L. Servadei, A. Maier, R. Wille, RadarSleepNet: Sleep pose classification via PointNet++ and 5D radar point clouds, in: 2023 IEEE Microwaves, Antennas, and Propagation Conference, MAPCON, IEEE, 2023, pp. 1–6.
[49] X. Liu, L. Yuan, C. Jiang, JiannanYu, Y. Li, Human identification using tooth based on PointNet++, in: Chinese Conference on Biometric Recognition, Springer, 2023, pp. 129–139.
[50] P. Liu, J. Golde, J. Morgenstern, S. Bodenstedt, C. Li, Y. Hu, Z. Chen, E. Koch, M. Neudert, S. Speidel, Non-rigid point cloud registration for middle ear diagnostics with endoscopic optical coherence tomography, Int. J. Comput. Assist. Radiol. Surg. 19 (1) (2024) 139–145.
[51] P. Kaftan, M.P. Heinrich, L. Hansen, V. Rasche, H.A. Kestler, A. Bigalke, Abstracting volumetric medical images with sparse keypoints for efficient geometric segmentation of lung fissures with a graph CNN, in: BVM Workshop, Springer, 2024, pp. 60–65.
[52] M. Zhu, Y. Quan, X. He, The classification of brain network for major depressive disorder patients based on deep graph convolutional neural network, Front. Hum. Neurosci. 17 (2023) 1094592.
[53] G. Sunil, S. Gowtham, A. Bose, S. Harish, G. Srinivasa, Graph neural network and machine learning analysis of functional neuroimaging for understanding schizophrenia, BMC Neurosci. 25 (1) (2024) 2.
[54] F. Gharebaghi, S.H. Sardouie, HFO detection from iEEG signals in epilepsy using time-trained graphs and deep graph convolutional neural network, in: 2024 32nd International Conference on Electrical Engineering, ICEE, IEEE, 2024, pp. 1–7.
[55] M. Tan, Q.V. Le, EfficientNet: Rethinking model scaling for convolutional neural networks, 2019, http://dx.doi.org/10.48550/ARXIV.1905.11946, arXiv, URL https://arxiv.org/abs/1905.11946.
[56] J. Hu, L. Shen, S. Albanie, G. Sun, E. Wu, Squeeze-and-excitation networks, 2017, http://dx.doi.org/10.48550/ARXIV.1709.01507, arXiv, URL https://arxiv.org/abs/1709.01507.
[57] G. Huang, Z. Liu, L. Van Der Maaten, K.Q. Weinberger, Densely connected convolutional networks, in: Proceedings of the IEEE Conference on Computer Vision and Pattern Recognition, 2017, pp. 4700–4708.
[58] E. Qiu, M. Vejdani-Jahromi, A. Kaliaev, S. Fazelpour, D. Goodman, I. Ryoo, V.C. Andreu-Arasa, N. Fujima, K. Buch, O. Sakai, Fully automated 3D machine learning model for HPV status characterization in oropharyngeal squamous cell carcinomas based on CT images, Am. J. Otolaryngol. 45 (4) (2024) 104357.
[59] M.H. Sadeghi, S. Sina, M. Alavi, Z.N. Feshani, A.H. Farshchitabrizi, 323: A comparison of 3D CNN architectures for monitoring ovarian cancer patients using PET/CT scans, Radiother. Oncol. 194 (2024) S4966–S4967.
[60] M.A. Talukder, M.A. Layek, M. Kazi, M.A. Uddin, S. Aryal, Empowering COVID-19 detection: Optimizing performance through fine-tuned EfficientNet deep learning architecture, Comput. Biol. Med. 168 (2024) 107789, http://dx.doi.org/10.1016/j.compbiomed.2023.107789.
[61] M. Aborokbah, Alzheimer's disease MRI classification using EfficientNet: A deep learning model, in: 2024 4th International Conference on Applied Artificial Intelligence, ICAPAI, IEEE, 2024, pp. 1–8, http://dx.doi.org/10.1109/icapai61893.2024.10541281.
[62] V. Kumar, C. Prabha, P. Sharma, N. Mittal, S.S. Askar, M. Abouhawwash, Unified deep learning models for enhanced lung cancer prediction with ResNet-50–101 and EfficientNet-B3 using DICOM images, BMC Med. Imaging 24 (1) (2024) http://dx.doi.org/10.1186/s12880-024-01241-4.
[63] H. Li, Y. Liang, Y. Liu, X. Xian, Y. Xue, H. Huang, Q. Yao, W. Liu, Development of an intelligent field investigation system for Liriomyza using SeResNet-Liriomyza for accurate identification, Comput. Electron. Agric. 214 (2023) 108276, http://dx.doi.org/10.1016/j.compag.2023.108276.
[64] J. Wang, Z. Luan, Z. Yu, J. Ren, J. Gao, K. Yuan, H. Xu, Superpixel segmentation with squeeze-and-excitation networks, Signal Image Video Process. 16 (5) (2022) 1161–1168, http://dx.doi.org/10.1007/s11760-021-02066-2.
[65] B.R. Devassy, J.K. Antony, Histopathological image classification using CNN with squeeze and excitation networks based on hybrid squeezing, Signal Image Video Process. 17 (7) (2023) 3613–3621, http://dx.doi.org/10.1007/s11760-023-02587-y.